Statistical analysis of dynamic behavior of continental shelf wave motions in the northern South China Sea

Junyi Li[1,2,3], Tao He[1,3], Quanan Zheng[1,4], Ying Xu[3], Lingling Xie[1*]

[1] Laboratory of Coastal Ocean Variation and Disaster Prediction, College of Ocean and Meteorology, Guangdong Ocean University, Zhanjiang 524088, China

[2] Key Laboratory of Climate, Sources and Environments in Continent Shelf Sea and Deep Ocean, Zhanjiang 524088, China

[3] Key Laboratory of Space Ocean Remote Sensing and Application, MNR, Beijing, 100081, China

[4] Department of Atmospheric and Oceanic Science, University of Maryland, College Park, MD 20742, USA

*Corresponding author.

E-mail address: L. Xie (xiell@gdou.edu.cn)

Abstract

This study aims to analyze statistical behavior of the continental shelf wave motions, including continental shelf waves (CSWs) and arrested topographic wave (ATW), in the northern South China Sea. The baseline consists of tide-gauge data from stations Kanmen, Xiamen, Shanwei, Hongkong, and Zhapo, as well as along-track sea level anomaly (SLA) data derived from multiple satellite altimeters from 1993 to 2020. The subtidal signals propagating along the coast with periods shorter than 40 d and phase speeds of about 10 m s^{-1} are interpreted as CSWs. The cross-shelf structure of along-track SLA indicates that mode 1 of CSWs is the predominant component trapped in the area shallower than about 200 m. The amplitudes of CSWs reach the maximum 0.6 m during July-September, and minimum 0.2 m during April-June. The inter-seasonal and seasonal signals represent ATWs. The amplitudes of ATWs reach 0.10 m during October-December, twice of that during July-September. These observations are well interpreted by the framework of linear wave theory. The cross-shelf structures of CSWs and ATWs derived from along-track SLA illustrate that the methods are suitable

for observing dynamic behavior of the CSWs.

1 Introduction

Continental shelf wave (CSW) is a type of topographic Rossby wave (TRW) trapped in the continental shelf with amplitudes ranging from several tens' centimeters to more than one meter (Aydın and Beşiktepe, 2022; Clarke and Brink, 1985; Heaps et al., 1988; Morey et al., 2006; Mysak, 1980; Robinson, 1964; Zheng et al., 2015). CSW is a sub-inertial motion with a wavelength much greater than the depth (Li et al., 2015; Schulz et al., 2011). It propagates along the shelf with the coast on its right (left) in the northern (southern) hemisphere (Clarke, 1977). During the impact of typhoon, an excessive flooding in the coastal zone could be induced by a propagating CSW that added to the locally wind-generated surge (Dukhovskoy and Morey, 2011; Han et al., 2012). Therefore, CSW is particularly important for coastal sea-level variations.

CSW is generally generated by large-scale weather systems moving across or along the shelf (Thiebaut and Vennell, 2010). CSW events have been reported by previous investigators lasted from 2 days to 2 weeks (Chen and Su, 1987; Li et al., 2015; Li et al., 2021; Zheng et al., 2015). The phase speed of CSWs depends on the bottom topography, ranging from 5 to 20 m s^{-1} (Li et al., 2015; Li et al., 2016; Shen et al., 2021). CSWs could be taken as barotropic motion in a homogeneous coastal area. While in a stratified ocean, it could be classified into coastal trapped wave. If the bottom boundary is flat, it propagates as a Kelvin wave. Overall, they are resulting from conserving potential vorticity over the shelf (Chen et al., 2022; Quan et al., 2021; Wang and Mooers, 1976).

The sea level variations in the South China Sea (SCS) are well depicted by these previous studies as the continental shelf occupies about its half area (Ding et al., 2012; Li et al., 2023b; Shen et al., 2021; Zhao et al., 2017; Zhou et al., 2023). However, two issues should be improved. The first is that the primary data are usually obtained from

60   the tide-gauge stations along the coastline. The data have high accuracies, but represent

61   the sea level at the coasts only. Thus, satellite-altimeter-observed the sea level variation

62   are often used to fill the data gaps in between the tide-gauge stations and on the

63   continental shelf. The second issue is that the repeated period of the satellite altimeter

64   is 9.9 d, which is challenging to investigate the sea level variations with periods shorter

65   than 10 d. Previous studies used the along-track sea level anomaly (SLA) from satellite

66   altimeters to describe CSW (Chen et al., 2014; Li et al., 2016). However, the satellite

67   altimeter with the sparse tracks (as shown in Fig. 1) could only capture the cross-

68   structure of CSW with one or two snapshot of one CSW.

69

70
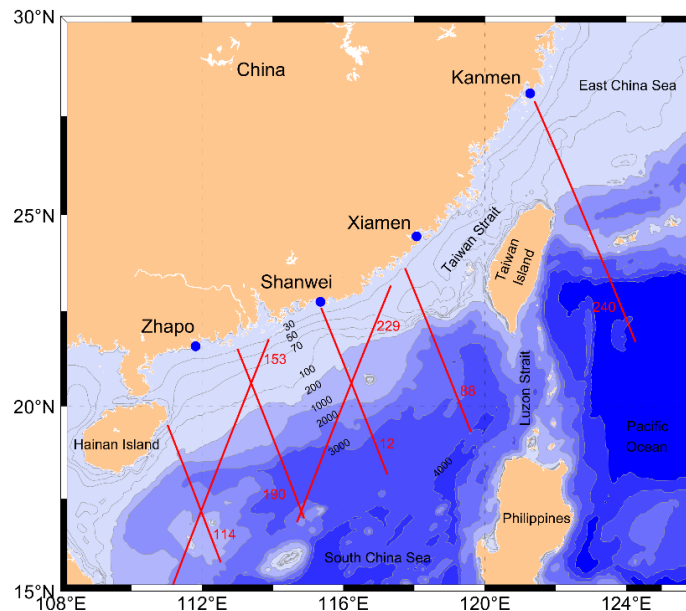
Fig. 1. Study area. Blue dots represent locations of tide-gauge stations Kanmen, Xiamen, Shanwei, and Zhapo. Red lines represent segments of ground tracks 12, 88, 114, 153, 190, 229, and 240 for altimeter satellites over the continental shelf. Tracks 12, 88,114, and 190 are almost perpendicular to the coastline. Isobaths are in m.

75

76   Under the background of global warming, the sea level variation with very low

77   frequency has been investigated by previous investigators. Ho et al. (2000) found

78   seasonal sea level variability in the SCS using data from a satellite altimeter. Kajikawa

79   and Yasunari (2005) investigated the interannual variability of the intra-seasonal

80   variation over the SCS. Fang et al. (2006) analyzed low sea level along the eastern

boundary of the SCS. Rong et al. (2007) investigated the relationship between ENSO (El Niño and Southern Oscillation) and interannual variability of sea level in the SCS. Zhuang et al. (2010) found strong intra-seasonal variability in the northern SCS. In addition, the sea level variations are influenced by thermodynamic processes, e.g., eddies and thermal change of upper layer of the SCS (Cheng and Qi, 2007; Xie et al., 2018; Zheng et al., 2014).

Meanwhile, the upper layer thermal changes significantly influence the sea level variations (Cheng and Qi, 2007). Wang et al. (2017) found that seasonal level anomalies are closely related to ENSO events (Wang et al., 2022). Using sea surface height (SSH) data from satellite altimeters, Xu et al. (2016) found that sea level variations in the coastal area of the SCS are still strongly influenced by the coastal current system in summer and winter. Seasonal circulation is mainly driven by the monsoon wind stress (Gan et al., 2006). Lin et al. (2021) applied the arrested topographic waves (ATWs) model to the coastal mean dynamic topography along the East China Sea (ECS) and SCS. The mean circulation in a coastal zone of variable depth may be modeled by linear equations (Wu, 2021). The result suggests that the mean dynamic topography is a counterbalance of contributions from the along-shelf wind and well predicted by the ATW model. Therefore, the monsoon winds are a control factor for the sea level variation.

This study aims to investigate the cross-shelf structures of sea level over the continental shelf. As the repeated period of the satellite altimeters, 9.9 d, is comparable with that of CSWs in the northern SCS, the statistical characteristics of the along-track SLA are applied to show the cross-shelf structure of CSWs using a long-term data set from 1993 to 2020. To figure out the cross-shelf structures of ATWs is another goal.

The rest of the paper is organized as follows: Section 2 describes the observed data. Section 3 presents theory of CSWs and ATWs. Section 4 presents the characteristics of the signals derived from the tide-gauge data and along-track SLA. Section 5 discusses the CSWs detected from tide-gauge data and the cross-shelf structure of sea level over the continental shelf. Section 6 gives summaries.

2 Data

2.1 Along-track sea level anomaly data

Satellite altimeter along-track SLA data are produced and distributed by the Archiving, Validation, and Interpretation of Satellite Oceanographic Data (AVISO), Centre National d'Etudes Spatiales (CNES) of France. The data from 1993 to 2020 are derived from TOPEX/Poseidon, Jason-1, Jason-2, and Jason-3 measurements. The satellite repetition period is 9.9 d, and the temporal resolution of the along-track data is 1 Hz. The along-track SLA is calculated by subtracting the twenty-year mean from the SSH measured by the satellite altimeters. The along-track SLA is low pass filtered using 7-point moving average. The ground tracks in the study area, 12, 88, 114, 153, 229, and 240, are shown in Fig. 1.

Satellite altimetry provides a unique sea level dataset to the coastal sea level research. A few recent studies have stressed the importance of small-scale coastal processed on coastal sea-level variance (Cazenave and Moreira, 2022; Vignudelli et al., 2019). The along-track SLA has been successfully validated and applied to the coast zone by Birol et al. (2021). These studies present the availability of along-track SLA in the coastal zones.

2.2 Sea level anomaly from tide-gauge

The tide-gauge data at stations Kanmen, Xiamen, Shanwei, Hongkong and Zhapo (as shown in Fig. 1) are obtained from the Global Sea Level Observing System (GLOSS). The data cover a period from 1993 to 1997, with a temporal resolution of 1 h. De-tided sea level anomaly (DSLA) is calculated by removing tidal signals using a Matlab toolbox (Pawlowicz et al., 2002).

The monthly sea level means at stations Xiamen, Shanwei, and Zhapo are obtained from the Permanent Service for Mean Sea Level (PSMSL). Monthly mean data cover periods of 1993-2003, 1993-1994, and 1993-2020 for stations Xiamen, Shanwei, and Zhapo, respectively.

2.3 Sea surface wind stress

Monthly sea surface wind stress is derived from the Copernicus Marine Environment Monitoring Service (CMEMS). The dataset covers a period from 1993 to 2020 with a spatial resolution of $0.25^{\circ} \times 0.25^{\circ}$. Sea surface wind stress data on the satellite altimeter ground tracks are decomposed into the cross-shelf and along-shelf components. The cross-shelf component is positive seaward and parallel to the satellite altimeter ground tracks (12, 88, 114 and 190). The along-shelf component is positive northward and perpendicular to these satellite altimeter ground tracks.

2.4 Topographic profile

The behavior of continental shelf waves is determined by the topography of the continental shelf and slope, which has been well documented. The topographic profiles along the satellite altimeter ground tracks are extracted from a dataset of ETOPO-2. This study uses one-dimensional linear piecewise functions to fit the topographic profiles along the satellite altimeter ground tracks. The width of the continental shelf, depths of shelf break and deep basin along the tracks are listed in Table 1. The continental shelf break is extracted as the location of maximum change in the gradient of continental slope.

Table 1. The width of the continental shelf, depths of shelf break and deep basin along the satellite ground tracks.

Track number	l(km)	H_1(m)	H_2(m)
12	200	-300	-3800
88	178	-200	-2500
114	123	-200	-1800
153	259	-110	-1600
190	247	-255	-3500
229	244	-225	-3500
240	273	-250	-5000

3 Theory

3.1 Momentum equation for CSWs

The linearized shallow-water equations governing a barotropic ocean on a rotating earth are

$$\frac{\partial u}{\partial t} - fv = -g\frac{\partial \eta}{\partial x} + \frac{\tau_s^x - \tau_b^x}{\rho H} \tag{1a}$$

$$\frac{\partial v}{\partial t} + fu = -g\frac{\partial \eta}{\partial y} + \frac{\tau_s^y - \tau_b^y}{\rho H} \tag{1b}$$

$$\frac{\partial \eta}{\partial t} + \frac{\partial (uH)}{\partial x} + \frac{\partial (vH)}{\partial y} = 0 \tag{1c}$$

where cross-shelf and along-shelf velocities (u, v) are depth-averaged in cross-shelf and along-shelf coordinates (x, y). η is the sea surface height. The Coriolis parameter is f. The bathymetry $H = H(x)$ is assumed to be a function of the cross-shelf variable, x only. τ_s and τ_b the surface and bottom stresses. g, ρ are the gravitational acceleration and the water density.

The scales of the along-shelf length of CSW ($L = 2\pi/k \approx 2 \times 10^3$ km), and cross-shelf length ($l \approx 200$ km) are subject to the long-wave assumptions ($l/L \ll 1$), i.e., $\partial u/\partial t = 0$ (Li et al., 2016; Schulz et al., 2011). Under this approximation, Eqs. (1a-b) become

$$v = \frac{g}{f}\frac{\partial \eta}{\partial x} - \frac{\tau_s^x - \tau_b^x}{f\rho H} \tag{2a}$$

$$u = -\frac{g}{f}\frac{\partial \eta}{\partial y} - \frac{\partial}{\partial t}\left(\frac{g}{f^2}\frac{\partial \eta}{\partial x} - \frac{\tau_s^x - \tau_b^x}{f^2 \rho H}\right) + \frac{\tau_s^y - \tau_b^y}{f\rho H} \tag{2b}$$

Substitute Eqs. (2a-b) into Eq. (1c), we obtain the equation governing SSH of CSWs

$$\frac{\partial}{\partial t}\left(\eta - \frac{gH}{f^2}\frac{\partial^2 \eta}{\partial x^2} - \frac{g}{f^2}\frac{\partial \eta}{\partial x}\frac{dH}{dx}\right) - \frac{g}{f}\frac{\partial \eta}{\partial y}\frac{dH}{dx} + \frac{\partial}{\partial x}\left(\frac{\tau_s^y - \tau_b^y}{f\rho}\right) + \frac{\partial^2}{\partial t \partial x}\left(\frac{\tau_s^x - \tau_b^x}{f^2 \rho}\right) - H\frac{\partial}{\partial y}\left(\frac{\tau_s^x - \tau_b^x}{f\rho H}\right) = 0 \tag{3}$$

Assume that CSWs are forced by along-shelf wind stress, i.e., $(\tau_s^x, \tau_s^y) = (0, \tau_s^y)$. The bottom friction is neglected to simplify the calculation in Eq. (3). Therefore, the equation governing the SSH of CSWs becomes

$$\frac{\partial}{\partial t}\left(\eta - \frac{gH}{f^2}\frac{\partial^2 \eta}{\partial x^2} - \frac{g}{f^2}\frac{\partial \eta}{\partial x}\frac{dH}{dx}\right) - \frac{g}{f}\frac{\partial \eta}{\partial y}\frac{dH}{dx} + \frac{\partial}{\partial x}\left(\frac{\tau_s^y}{f\rho}\right) = 0 \tag{4}$$

The change in the SSH of CSWs is balanced by the variation of along-shelf wind stress in cross-shelf direction. Assume a periodic along-shelf wind stress, $\tau_s^y = \tau_0 \exp[i(\alpha y + \omega t)]$ (where α is wavenumber of wind stress, and $\tau_0 =$ constant). Eq.

191   (4) becomes

$$\frac{\partial}{\partial t}\left(\eta - \frac{gH}{f^2}\frac{\partial^2 \eta}{\partial x^2} - \frac{g}{f^2}\frac{\partial \eta}{\partial x}\frac{dH}{dx}\right) - \frac{g}{f}\frac{\partial \eta}{\partial y}\frac{dH}{dx} = 0 \tag{5}$$

193   which means that the change in SSH is independent of along-shelf wind stress.

194   The assumption of a wave solution

$$\eta = \phi(x)\exp[i(ky + \omega t)] \tag{6}$$

196   yields an equation for $\phi(x)$,

$$H\frac{d^2 \phi}{dx^2} + \frac{dH}{dx}\frac{d\phi}{dx} + \left(\frac{fk}{\omega}\frac{dH}{dx} - \frac{f^2}{g}\right)\phi = 0 \tag{7}$$

198

199   3.1.1 Over the shelf

200   For $0 \leq x \leq l$, $H = H_1 x/l$, the equation for $\phi(x)$ is

$$x\frac{d^2 \phi}{dx^2} + \frac{d\phi}{dx} + \left(\frac{fk}{\omega} - \frac{f^2 l}{gH_1}\right)\phi = 0 \tag{8}$$

202   which is subject to the following boundary conditions: $\phi(0) = a$, and $\phi(l) = A$. a and

203   A should be arbitrary. We could take a as the amplitude of fluctuation in sea level from

204   the tidal gauge station.

205   The solution to Eq. (8) is expressed as the sum of the first and second kinds of

206   Bessel functions (Robinson, 1964; Schulz et al., 2011)

$$\phi(x) = aJ_0\left(2\left(\frac{fk}{\omega} - \frac{f^2 l}{gH_1}\right)^{\frac{1}{2}} x^{\frac{1}{2}}\right) + bY_0\left(2\left(\frac{fk}{\omega} - \frac{f^2 l}{gH_1}\right)^{\frac{1}{2}} x^{\frac{1}{2}}\right) \tag{9}$$

208   where a is arbitrary constant. As the solution for $\phi(x)$ is finite, therefore

$$\phi(x) = aJ_0\left(2\left(\frac{fk}{\omega} - \frac{f^2 l}{gH_1}\right)^{\frac{1}{2}} x^{\frac{1}{2}}\right) \tag{10}$$

210

211   3.1.2 In the deep basin

212   For $l < x$, $H = H_2$, the equation for $\phi(x)$ is

$$\frac{d^2 \phi}{dx^2} - \frac{f^2}{gH_2}\phi = 0 \tag{11}$$

214   which is subject to the following boundary conditions: $\phi(x \to l) = A$, and $\phi(\infty) = 0$.

215   The solution is

216 $$\phi(x) = A \exp\left(-\frac{fl}{\sqrt{gH_2}}\left(\frac{x}{l} - 1\right)\right) + B \exp\left(\frac{fl}{\sqrt{gH_2}}\left(\frac{x}{l} - 1\right)\right) \tag{12}$$

217 As the solution for $\phi(x)$ is also finite in the deep basin, i.e.,

218 $$\phi(x) = A \exp\left(-\frac{fl}{\sqrt{gH_2}}\left(\frac{x}{l} - 1\right)\right) \tag{13}$$

219 where A is arbitrary constant.

220

221 3.1.3 Dispersion relation

222 As the fluid is continuous at the edge of continental shelf, therefore

223 $$H_1 \cdot u|_{x \to l_-} = H_2 \cdot u|_{x \to l_+} \tag{14a}$$

224 $$a J_0 \left(2 \left(\frac{fkl}{\omega} - \frac{f^2 l^2}{gH_1}\right)^{\frac{1}{2}}\right) = A \tag{14b}$$

225 From Eq. (14a), we have

226 $$H_1 \cdot a \left(k J_0 + \frac{\omega}{f}\left(\frac{fk}{\omega l} - \frac{f^2}{gH_1}\right)^{\frac{1}{2}} J_0'\right) = H_2 \cdot A \left(k - \frac{\omega}{\sqrt{gH_2}}\right) \tag{15}$$

227 where J_0' is the derivation of the zero-order of the first kind Bessel function,

228 $$J_0'(x) = -\frac{x}{2}\left(J_0(x) + J_2(x)\right) \tag{16}$$

229 where J_2 is the second order of J_0.

230 Substituting Eq. (16) into Eq. (15) yields a dispersion relation for CSWs

231 $$\left(\frac{cfl}{gH_2} - 1 + \frac{c}{(gH_2)^{\frac{1}{2}}}\right) J_0 - \left(\frac{H_1}{H_2} - \frac{cfl}{gH_2}\right) J_2 = 0 \tag{17}$$

232 where $c \,(= \frac{\omega}{k})$ is phase speed of CSWs. We solve Eq. (17) using the zero-finding
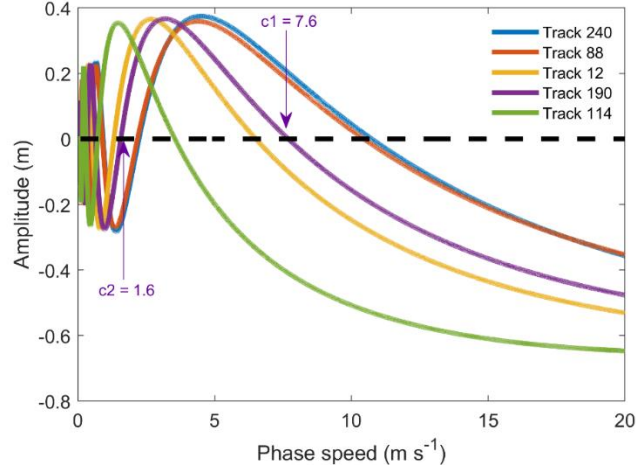
233 function in MATLAB. The solution of phase speed for CSWs is shown as Fig. 2. The

234 zero-crossing points for each curve present the phase speed of CSWs. The first zero-

235 crossing point on the right hand of each curve points out the phase speed of mode-1

236 CSW, e.g., $c = 7.6$ m s^{-1} for track 190.

237

Fig. 2. Solution of phase speed for CSWs from Eq. (17). The zero-crossing values represent the phase speed of CSWs for different modes. Colorful curves are amplitude of zero-order of the first kind Bessel function in different modes for the idealized depth profile of tracks 12, 88, 114, 190, and 240, respectively. Arrows point out the phase speed of mode-1 (7.6 m s^{-1}) and mode-2 (1.6 m s^{-1}) CSWs along track 190.

3.1.4 Cross-shelf structure

With Eqs. (10), (13) and (14b), the wave solution of SSH, i.e., Eq. (3), is

$$\eta = \begin{cases} \sum_{i=1}^{\infty} a_i \cdot J_0 \left(2 \left(\frac{fk_i}{\omega_i} - \frac{f^2 l}{gH_1} \right)^{\frac{1}{2}} x^{\frac{1}{2}} \right) \exp[i(k_i y + \omega_i t)] & x \le l \\ \sum_{i=1}^{\infty} a_i \cdot J_0 \left(2 \left(\frac{fk_i l}{\omega_i} - \frac{f^2 l^2}{gH_1} \right)^{\frac{1}{2}} \right) \exp\left(-\frac{fl}{\sqrt{gH_2}} \left(\frac{x}{l} - 1 \right) \right) \exp[i(k_i y + \omega_i t)] & x > l \end{cases}$$

(18)

where $\exp[i(ky + \omega t)]$ is the waveform propagating along the shelf. $a_i \cdot J_0$ is the cross-shelf structure of the waveform for mode i over the shelf.

In the cross-shelf direction, the SSH becomes

$$\eta = \begin{cases} \sum_{i=1}^{\infty} \eta_{0i}(t) \cdot J_0 \left(2 \left(\frac{fk_i}{\omega_i} - \frac{f^2 l}{gH_1} \right)^{\frac{1}{2}} x^{\frac{1}{2}} \right) & x \le l \\ \sum_{i=1}^{\infty} \eta_{0i}(t) \cdot J_0 \left(2 \left(\frac{fk_i l}{\omega_i} - \frac{f^2 l^2}{gH_1} \right)^{\frac{1}{2}} \right) \exp\left(-\frac{fl}{\sqrt{gH_2}} \left(\frac{x}{l} - 1 \right) \right) & x > l \end{cases} \quad (19)$$

where $\eta_{0i}(t) \ (= a_i \exp[i(k_i y + \omega_i t)])$ is time series of SSH at the coastline for mode i.

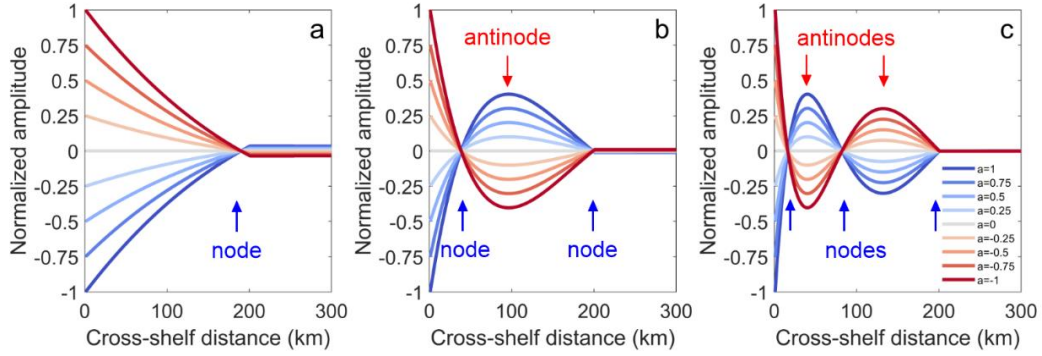Fig. 3 shows the SSH evolution over the continental shelf. The SSH mode 1 looks like a bell mouth. For Modes 2 and 3, nodes and antinodes appear on the shelf. Node for Mode 2 appears at 50 km off the coast over the shelf. Nodes for Mode 3 appear at

10

258   30 and 90 km off the coast.

259

Fig. 3. (a-c) Cross-shelf structure of normalized amplitudes of the first three CSW modes for idealized depth profile of track 12. Gradient color curves represent amplitude evolution over time for CSWs in the cross-shelf direction.

3.2 Steady situation

The governing equations in the steady situation for Eqs. (1a-c) are

$$-fv = -g\frac{\partial\eta}{\partial x} \tag{20a}$$

$$fu = -g\frac{\partial\eta}{\partial y} + \frac{\tau_s^y - \tau_b^y}{\rho H} \tag{20b}$$

$$\frac{\partial(uH)}{\partial x} + \frac{\partial(vH)}{\partial y} = 0 \tag{20c}$$

A linear drag is used for the bottom friction, i.e., $\vec{\tau_b} = \rho\lambda\vec{u}$ (Hsueh and Pang, 1989; Lin and Yang, 2011).The SSH Eqs. (20a-c) becomes (Csanady, 1978)

$$\eta = B\tau_0 e^{-\frac{x}{L}}\sin\left(\alpha y + \frac{x}{L} - \frac{\pi}{4}\right) \tag{21}$$

where $L = \sqrt{2\lambda l/\alpha f H_1}$ is the scale width of trapped sea level in the cross-shelf direction, B is an arbitrary constant. A drag coefficient, $\lambda = O(5 \times 10^{-4})$ m s^{-1}, is used for the linear bottom friction (Chapman, 1987; Lin and Yang, 2011). The typical magnitude for winter wind stress over the northern continental shelf of the SCS is $O(0.1)$ N m^2 (Lin and Yang, 2011; Lin et al., 2011). $f = 5 \times 10^{-5}$ s^{-1}, and $\alpha = 2\pi/4000$ km evaluated by Lin et al. (2021).

The normalized SSH in the cross-shelf direction of ATW for tracks 12, 88, 114, and 190 are shown in Fig. 4. One can see that the trapped sea level in the cross-shelf direction decays quickly from 1 at the coastline to ~0.2 at the edge of the continental

282   shelf (~200 km), and 0.1 at a distance of 300 km. The ATW amplitude decays offshore

283   with a scale equal to the deformation radius, and $L = {\sim}100$ km in the study area, which

284   is much less than the local Rossby radius of deformation (~600 km). Under different

285   wind stresses, the amplitude of ATW evolves similarly to that in Fig. 3a. As Track 240

286   is not perpendicular to the coastline, it is beyond the scope.

287
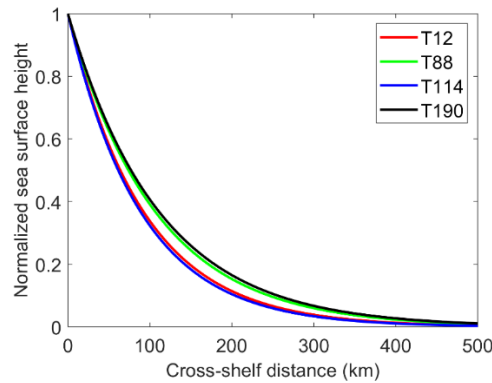
288

289 **Fig. 4.** Normalized SSH in cross-shelf direction for tracks 12, 88, 114, and 190.

290

291 **4 Signals in sea level anomaly**

292 4.1 Tide-gauge data

293   Fig. 5 shows the wavelet transform (WT) of SLA at station Xiamen from 1993 to

294   1997. One can see abundant signals with periods from several days to one year in Figs.

295   5a-b. A dozen signals with periods from several days to about one month could be seen

296   from the WT of SLA every year. The duration of these signals, with a period of several

297   days, is about ten days (e.g., in Fig. 5d). Moreover, the signals with a period of about

298   one month sustain for about three months (Figs. 5c-d). Even if significance level against

299   red noise is larger than 5%, the power is universal and continuous in the period bands

300   of 10-60 d. The main reason is that these signals are not so significant compared with

301   the signals with large amplitude. The wavelet analysis also exhibits a significant inter-

302   seasonal and seasonal variation of SLA. The characteristics of the signals at stations

303   Kanmen, Shanwei, and Zhapo are almost the same (not shown here). Therefore, the

304   variation of SLA along the northern SCS coast is universal.

305
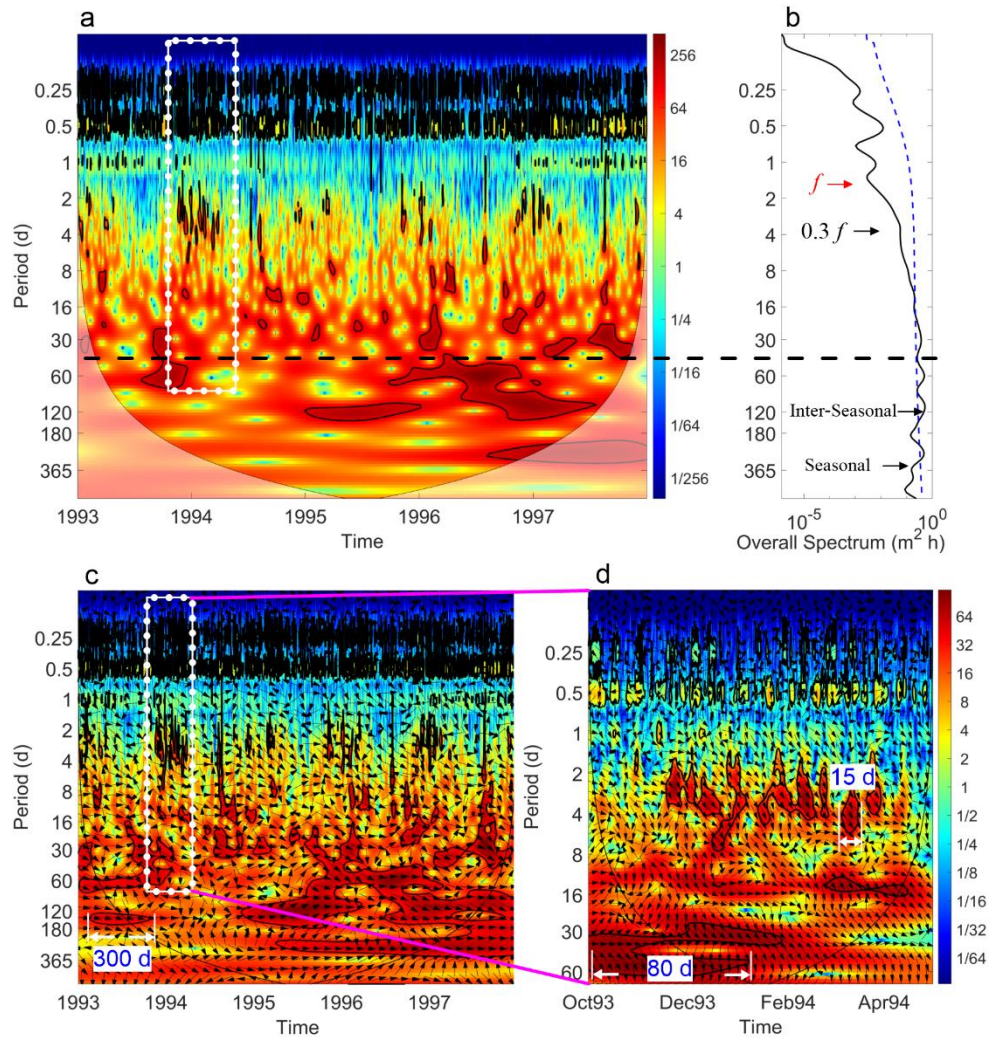
Fig. 5. Temporal variability of SLA at the coastline. (a) WT of SLA at station Xiamen. (b) Overall spectrum of SLA at station Xiamen. (c) XWT of SLA between stations Kanmen and Xiamen. (d) XWT of SLA between stations Kanmen and Xiamen from October 1993 to April 1994. White line and arrows are auxiliary lines pointed out duration. The thick line is a 5% significance level against red noise, and the cone of influence (COI) is shown as the thin line. Color codes of power spectra normalized by variance are in arbitrary units. White dotted rectangles in (a) and (c) show the temporal domain of (d). The Blue dashed curve in (b) is a 5% significance level. Arrows in (b) point out the characteristic frequencies of inertial oscillation and CSWs. The black dashed lines in (a) and (b) represent signal period boundary (40 d). The arrows in (c) and (d) show the relative phase relationship between SLA at Kanmen and Xiamen with in-phase (anti-phase, leading, and lagging) pointing right (left, down, and up).

Figs. 5c-d show the cross wavelet transform (XWT) of SLA between stations Kanmen and Xiamen. One can see that the period band and the occurrence time of the significant cross wavelet power are consistent with that in Fig. 5a. The signals with

periods shorter and longer than 40 d show remarkably different characteristics. In the period band shorter than 40 d, one can see the arrows point bottom left uniformly. The uniform phase lag indicates the fixed time delay of the signal between two tidal gauge station. While, the direction of arrows is in disorder in the lower period band, which indicates there is no evidence for propagating.

In the period band shorter than 40 d, the signals at station Xiamen lag that at station Kamen about 15 h. The propagation phase speed of the sea level signal could be calculated by the lag time of sea level propagation between stations Kanmen and Xiamen. The result is about 9 m s^{-1}, which is very close to that reported by a number of recent studies (Ding et al., 2012; Li et al., 2015; Li et al., 2016; Zhao et al., 2017).

In the period band longer than 40 d, the phase of signals between Kanmen and Xiamen is a little complicated. The signal phase with the period of 360 d from 1995 to 1997 is almost 0. However, the seasonal signals at station Xiamen lag (lead) that at station Kanmen in winter (summer) about $\pi/4$-$\pi/2$, implying that the signal propagates very slowly along the coast. Csanady (1978) concluded that these signals are a kind of ATWs.

4.2 Along-track SLA

Fig. 6 shows the latitude distribution of along-track SLA over the northern continental shelf of the SCS from 1993 to 2020. One can see the clear annual signals near the coast in Figs. 6a-g. Signals with periods shorter than one year could also be seen. As shown in Figs. 6h-n, a clear seasonal cycle is discernable from the climatological monthly mean of along-track SLA. One can see that lower (higher) sea levels over the shelf exist from March to August (September to February). The trough (~-0.2 m) and peak (~0.24 m) of sea level near the coast occur in July and October, respectively. While in track 240, climatological monthly mean of along-track SLA on the shelf is smaller than that in track 88 especially in July. The 28-year mean value of along-track SLA is about 0.04 m, as shown in Figs. 6o-u.
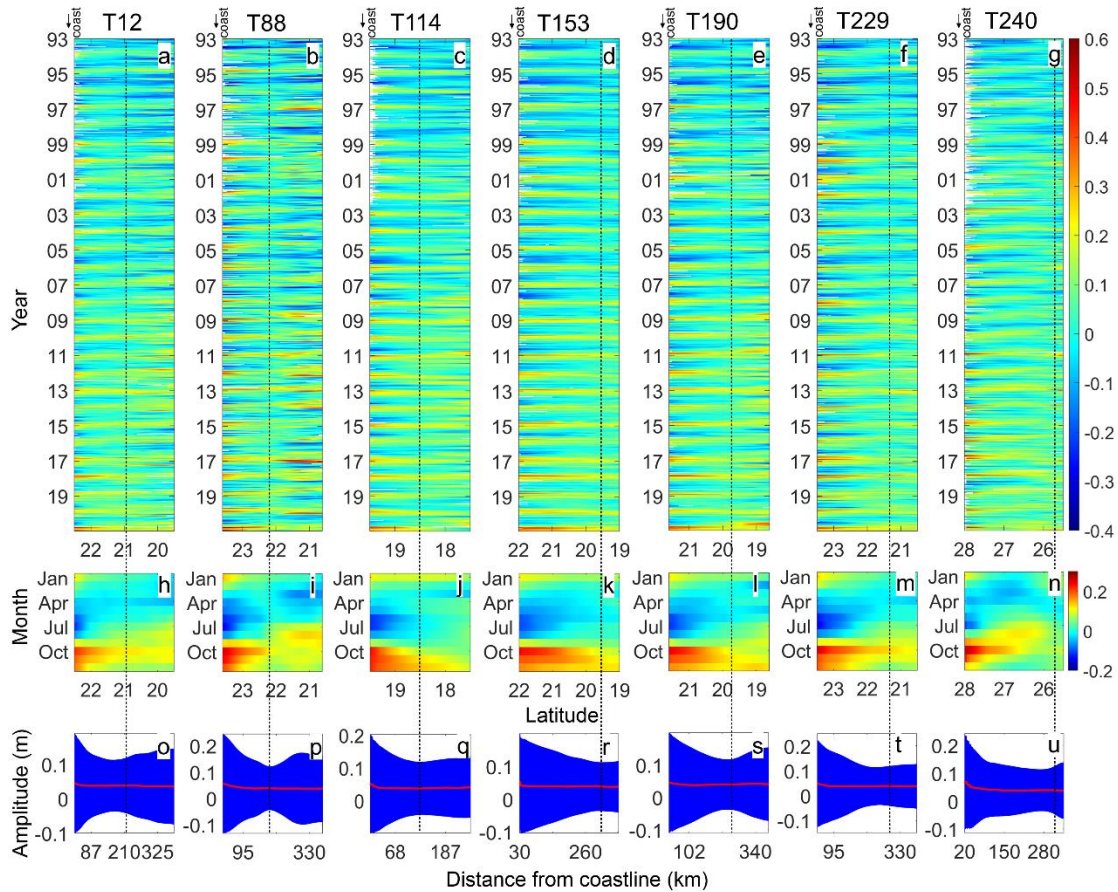
Fig. 6. (a-g) Latitudinal distribution of along-track SLA over the northern continental shelf of the SCS from 1993 to 2020 for tracks 12, 88, 114,153, 190, 229, and 240, respectively. (h-n) Climatological monthly mean of along-track SLAs for Tracks 12, 88, 114,153, 190, 229, and 240. (o-u) Mean (red curves) and standard deviation (blue shadow) of along-track SLA from 1993 to 2020 for tracks 12, 88, 114,153, 190, 229, and 240.Track numbers are shown on the tops of panels. Vertical dashed lines represent shelf break positions along the tracks, i.e., H_1, listed in Table 1. The coastline position is marked by an arrow on top left of each panel.

Moreover, the standard deviations (STD) of along-track SLA from 1993 to 2020 (blue shadow in Figs. 6o-u) show a bell-mouth-like structure over the shelf. The amplitudes of along-track SLA reach the maxima near the coast. The minimum variance exists near the shelf edge. The cross-shelf structure of SLA indicates that sea-level signals depend on the shelf depth.

5 Discussion

5.1 Propagation of CSWs

Fig. 7 compares the data derived from the XWT of SLA with the dispersion

15

371 relation of CSW. We overlay the dispersion relation curves of CSWs with the results

372 (phase speed, c and period, T, $\lambda = c \cdot T$) from tide-gauge data analysis in Section 4.1.

373 One can see that the data points derived from station pairs are distributed near the

374 dispersion relation of CSWs, implying the signals with the periods shorter than 40 d are

375 the CSWs propagating along the shelf.

376
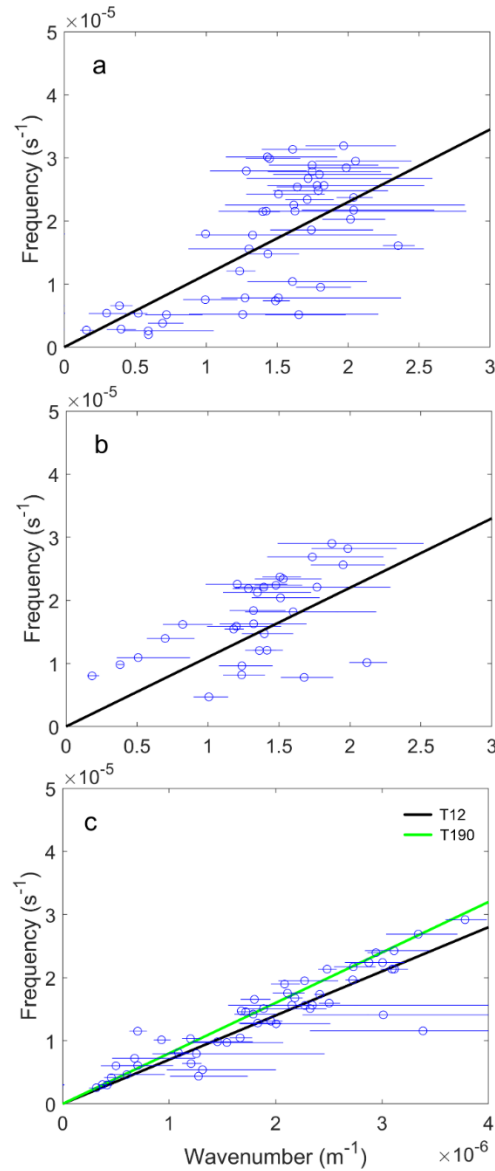
377

378 **Fig. 7.** Dispersion relation of the lowest mode of CSWs between (a) Kanmen and
379 Xiamen, (b), Xiamen and Shanwei, as well as (c) Shanwei and Zhapo. The data points
380 are calculated from the XWT of SLA. The curves are the theoretical dispersion relation
381 for the mean depth profiles listed in Table 1. Black and green curves in (c) represent the
382 dispersion relation (from Fig. 2) for the topographic profiles along tracks 12 and 190

383

384   Figs. 7a-b deal with the signals between Kanmen and Shanwei. We use the

385   bathymetric profile near Track 240 and 88 of the altimeter satellite to calculate the

386   dispersion relation curve, respectively. However, since the topography between

387   Kanmen and Shanwei changes dramatically, the data points lie dispersedly around the

388   curve. The wavenumbers of CSWs range from 0.1 to 2.4 $\times 10^{-5}$ m^{-1} between stations

389   Kanmen and Shanwei. The CSWs propagate along the coast with a phase speed of 10

390   m s^{-1}.

391   Fig. 7c shows the signals between Shanwei and Zhapo. The data points and the

392   theoretical curves agree quite well. Compared with the topography between Kanmen

393   and Shanwei, the topography changes slightly between stations Shanwei and Zhapo.

394   Thus, we conclude that the signals in tide-gauge data with the periods shorter than 40

395   d are the CSWs propagating along the shelf. The phase speed of CSWs is about 8 m s^{-}

396   ^{1} in the study area, which is close to that of previous studies (Li et al., 2015; Li et al.,

397   2016; Shen et al., 2021).

398   Previous studies present that the periods of CSWs range from two days to two

399   weeks in the SCS (Chen and Su, 1987; Li, 1993). The period of CSWs upstream, i.e.,

400   in the ECS, is often detected as several days (Ding et al., 2012; Ding et al., 2018; Hsueh

401   and Pang, 1989; Huang et al., 2015; Yin et al., 2014). Hsueh and Romea (1983) found

402   the sea level fluctuations with a period more than 13 d along the West Korean coast.

403   Worldwide, these low-frequency CSWs are common along the coast of Chile and the

404   east coast of the Indian Ocean (Castro and Lee, 1995; Hormazabal et al., 2001; Marshall

405   and Hendon, 2013; Vialard et al., 2009), where the width of the continental shelf is

406   narrow. In this study, we define the CSW with a maximum period of about 30-40 d. The

407   main reason for the difference is data length we used. The long-time series of DSLA

408   helps analyze the abnormal low-frequency CSWs in the SCS.

409   In addition, we should take care that CSWs in Fig. 7 are mixed with wind-forced

410   CSWs. It is difficult to separate the effect of wind-force and free propagating CSWs

411   clearly. Hsueh and Romea (1983) found that there is clear coupling between surface

412   winds and coastal sea level in the northeast China Sea. Li et al. (2016) found that the

413   propagation time of the wind signals are much shorter than that of CSWs in the north

414 SCS. Even one can see isolated cases which are away from dispersion relationship of

415 CSW in Fig. 7, most of the data points are near the theoretical dispersion relation.

416 Moreover, the stratification in the continental shelf is important for the characteristics

417 of CSW. The sea level variation in this study should present baroclinic and barotropic

418 CSWs in the shelf area together.

419

420 5.2 Trapped cross-shelf structure

421 5.2.1 CSWs

422   As the sampling period of the altimeter satellites is about 10 d, the signals with the

423 periods shorter than 20 d could not be distinguished from the along-track SLA based

424 on the Nyquist sampling theorem. Fortunately, the cross-shelf structure of CSWs could

425 be sampled as fragments by repeated satellite observations.

426   In this case, the CSWs with a period less than 40 d were abundant from 1993 to

427 2020 on the northern continental shelf of the SCS, especially in winter (Fig. 5). Even if

428 the significance level is larger than 5%, the power is universal and continuous in this

429 period band. Therefore, it could be considered that a large number of repeated

430 observations by altimeter satellites were executed during CSW events.

431   Fig. 8 shows a boxplot of along-track SLA over the continental shelf for tracks 12,

432 88, 114, and 190. The maxima, minima, and outliers derived from Fig. 8 are listed in

433 Table 2. The whisker dashed black line outside of the box extends to the most extreme

434 data points, not considering the outliers at the 5 % significance level. One can see that

435 the trapped characteristics as the maximum amplitude (75th percentile), interquartile

436 range (IQR), and outliers (red plus sign) occur at the coastal side. In contrast, the

437 minima occur at the edge of the continental shelf (150, 165, 105 and 165 km offshore

438 for tracks 12, 88, 114 and 190). The amplitude of along-track SLA for maxima and IQR

439 decreases gradually from the coastline (0.2-0.4 m) to the edge of the continental shelf

440 (~0.1 m). The largest outlier is 0.65 m over the shelf 30 km offshore.

441
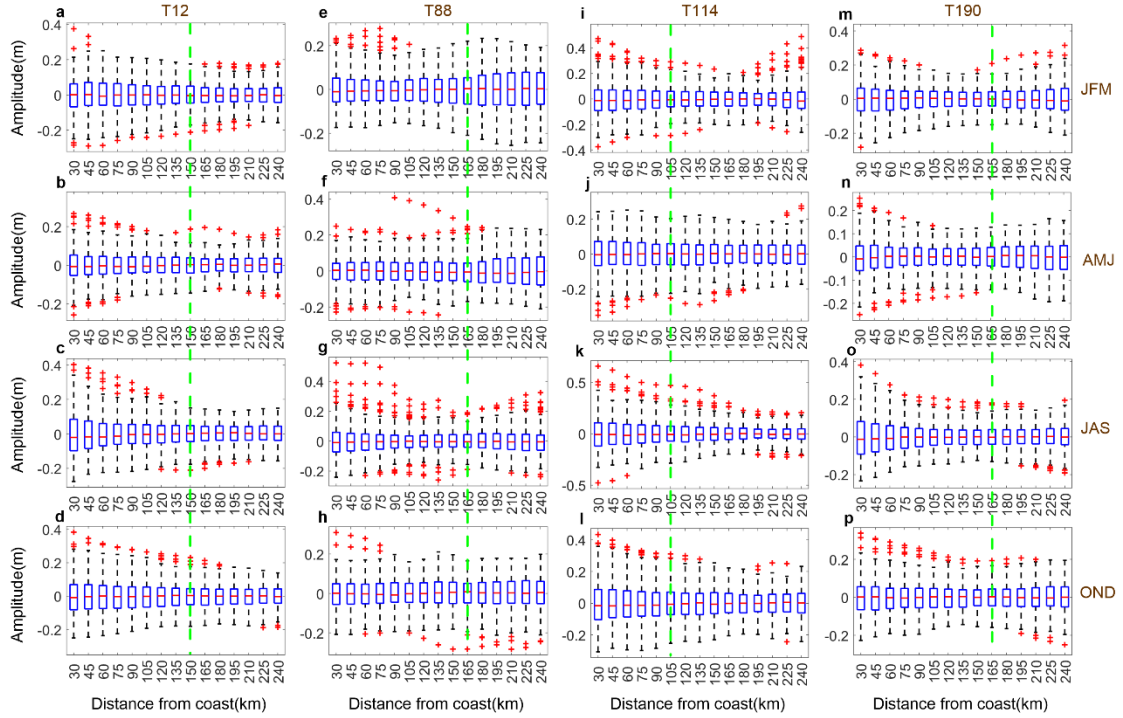
442

443 **Fig. 8.** Boxplot of along-track SLA on the shelf for tracks 12, 88, 114, and 190 from
444 1993 to 2020 (in the column). Seasonal means of SLA are plotted in the rows. Green
445 dashed lines present the minimum STD of the along-track SLA. The climatological
446 seasonal mean is removed. The along-track SLA is cut into small segments for every
447 15 km offshore, and averaged in each segment.

448

449 Table 2. Parameters extracted from along-track SLA in Fig. 8.

Position *	Track (Distance)**	T12 (150 km)				T88 (165 km)				T114 (105 km)				T190 (165 km)			
	Month	JFM	AMJ	JAS	OND	JFM	AMJ	JAS	OND	JFM	AMJ	JAS	OND	JFM	AMJ	JAS	OND
Coast	Outlier(m)	0.28	0.25	0.38	0.34	0.47	-0.35	0.65	0.43	0.23	0.24	0.52	0.31	0.38	0.27	0.41	0.38
	Maxi(m)	0.26	0.19	0.32	0.24	0.29	0.24	0.42	0.36	0.21	0.17	0.25	0.18	0.21	0.19	0.34	0.28
	Mini(m)	-0.23	-0.22	-0.24	-0.23	-0.3	-0.24	-0.33	-0.31	-0.17	-0.18	-0.24	-0.2	-0.25	-0.21	-0.28	-0.25
Edge	Outlier(m)	0.17	-0.15	0.19	0.19	0.23	-	0.29	-	0.21	0.39	0.28	0.16	-0.2	0.2	-0.2	0.21
	Maxi(m)	0.15	0.12	0.13	0.16	0.16	0.2	0.2	0.22	0.17	0.18	0.15	-0.18	0.16	0.12	0.14	0.17
	Mini(m)	-0.15	-0.14	-0.13	-0.15	-0.19	-0.2	-0.2	-0.21	-0.16	-0.14	-0.15	-0.2	-0.17	-0.13	-0.16	-0.17

450 *Coast is the position with the highest STD for each track, about 15 km offshore. Edge
451 is the position with the minimum STD of along-track SLA as shown in Fig. 8.
452 ** Distance between coastline and edge.

19

453

The largest SLA over the shelf occur from July to September. For example, the 75th percentile of SLAs near the coastline is about 0.25 m for track 144, and 0.42 m for track 88. The largest outlier of 0.65 m also occurs from July to September for track 88. The smallest SLA occurs from April to June when the wind is weak during the monsoon transition period (Wang et al., 2009). The extreme data from July to September show the occurrences of storm surges over the shelf (Chen et al., 2014).

Overall, the maximum amplitude, IQR, and extreme data of the along-track data over the shelf show the trapped wave characteristics, which shows that SLA decreases gradually from the coastline to the edge of the continental shelf. The trapped characteristics from the along-track SLA are similar to the cross-shelf structure of normalized amplitudes of the mode 1 CSWs, as shown in Fig. 3a. It should contain higher modes in the along-track SLA. The along-track SLA along tracks 153 and 229 show similar characteristics (not shown). That along track 240 (as shown in Fig. 6n) presents a differentiated pattern in the coast side and shelf edge during May-July. The main reason should be the existence of cold eddy in the north of Taiwan Island.

To further reveal the variations in the along-track SLA in track 12 on the shelf, the empirical orthogonal function (EOF) analysis results are shown in Fig. 9 (EOF analysis for data along other tracks is similar, not shown here). The first four EOF modes of the along-track SLA explain 96.8% of the total variance. Mode 1 explains the seasonal variance of SSH (red curve in Figs. 6o-u). The seasonal cycle could be characterized clearly from Fig. 9b, with peaks in October and troughs in May. Mode 2 and Mode 3 are similar to the cross-shelf structure as shown in Fig. 3a, which explains 25.1% of the total variance. Mode 3 is influenced by the background of SSH in the open sea side. The amplitude is 0.3-0.4 m, which is comparable to the outlier data as shown in Table 2. Mode 4 is similar to the cross-shelf structure of mode-2 CSW as shown in Fig. 3b, which only explains 2.8% of the total variance. The EOF analysis indicates that CSW could explain <30% of the total variance of SSH in the study area, which is comparable to the IQR in boxplot of along-track SLA (Fig. 8).

482
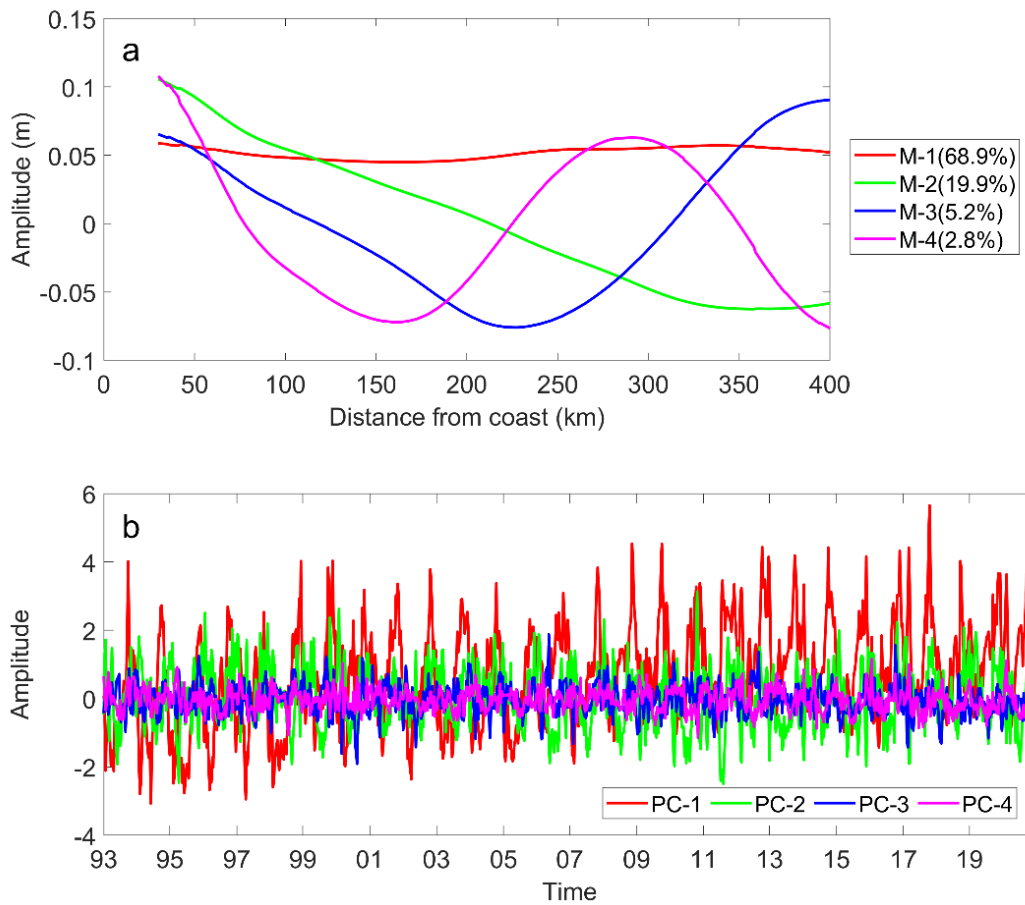
**Fig. 9.** The first four EOFs for along-track SLA on the shelf along track 12. Cross-shelf amplitude (a) and time series (b) of EOFs. The variance explained by each mode is labeled in (a).

5.2.2 ATWs

As shown in Fig. 6, the inter-seasonal and seasonal signals could be distinguished from along-track SLA. Fig. 10 shows the seasonal mean of along-track SLA and along-shelf sea surface wind. One can see that the time series of the seasonal mean of along-track SLA show the seasonal variation with the amplitude of 0.1-0.2 m at 15 km offshore. The time series of the seasonal mean of DSLA show similar characteristics with along-track SLA. The correlation relationship between the seasonal mean of along-track SLA and along-shelf sea surface winds reaches >0.77. The monthly mean of SLA during April-September is negative, while positive in the other months. It is attributed to that the local wind stress substantially influences the coastal sea level (Lin

21

499
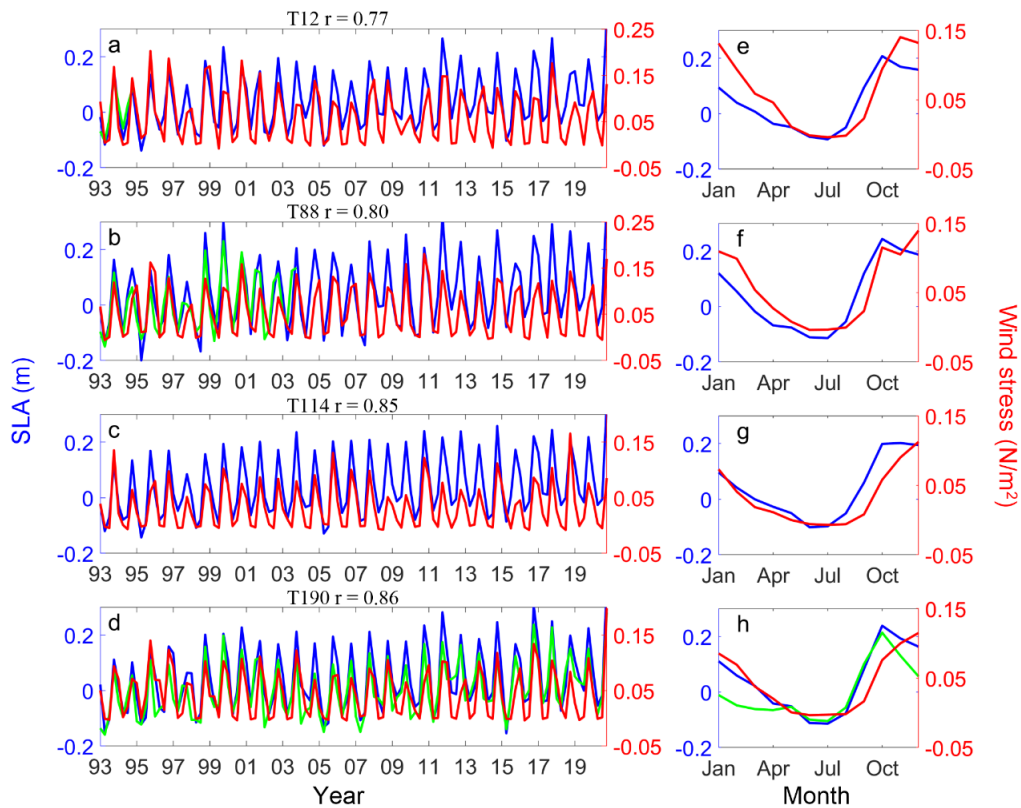
Fig. 10. Time series of the seasonal mean of along-track SLA and along-shelf sea surface wind stress for tracks (a)12, (b) 88, (c) 114, (d)190, and (e-h) monthly climatological mean of along-track SLA and along-shelf sea surface wind stress. Red curves represent the along-track SLA at 15 km offshore. Green curves represent the seasonal mean of sea level data at tide-gauge stations (a) Xiamen, (b) Shanwei, and (d) Zhapo.

507

In addition, one can also see a characteristic of out of sync between seasonal mean of along-track SLA and wind. The maximum of mean sea surface wind stress occurs in November and December. While, that of monthly along-track SLA occurs in October. Ding et al. (2020) investigated the seasonality of coastal circulation in the north SCS using a numerical model. The result indicates that the maximum of water transport is 1.93 Sv occurred in autumn. Li et al. (2023a) found the along-shelf current is strongest in October at approximately $0.17\,\mathrm{m\,s^{-1}}$. The along-shelf current involves with ATW, which is the reason why there is a difference between monthly climatological mean of along-track SLA and sea surface wind stress as shown in Figs. 10e-h.

Fig. 11 shows the cross structure of the seasonal mean of along-track SLA. One can see that the SLA on the coastline side is lower than on the ocean side from April to September. In the other seasons, the slope of along-track SLA is the opposite. The along-track SLA presents similar characteristics as shown in Fig. 10, i.e., the variation of SLA is controlled by the sea surface winds over the shelf.
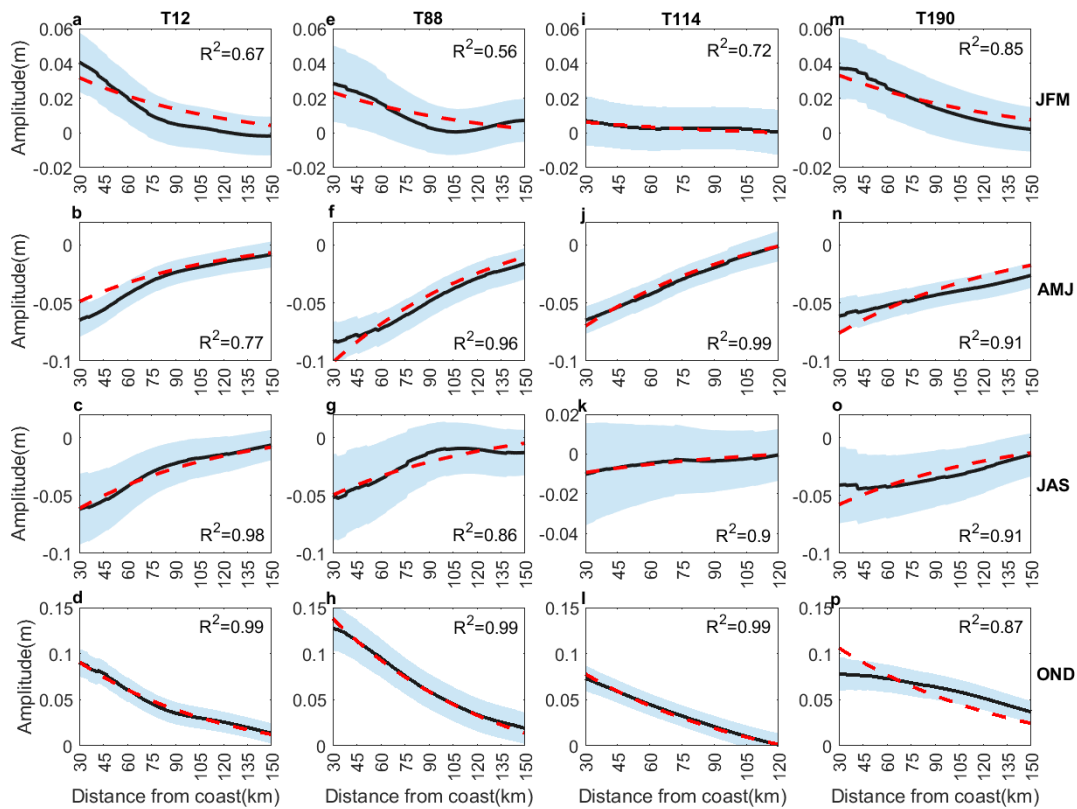
Fig. 11. Fitting climatologic seasonal mean of along-track SLA (black curves) using cross-shelf ATWs (red dashed curves) for tracks (a-d) 12, (e-h) 88, (i-l) 114, and (m-p) 190. Dashed shadow is the STD of the seasonal mean of along-track SLA.

Meanwhile, from Fig.11 one can see the cross-shelf structure of along-track SLA. The fitting curves show that theoretical ATWs (Fig. 4) explains the cross-shore structure of along-track SLA very well. The amplitudes of ATWs in track 12 are 0.04 m, -0.06 m, -0.05 m, and 0.10 m in January-March, April-June, July-September, and October-December. That along track 88 is relatively larger, e.g., 0.13 m in October-December. While, the minimum amplitude occurs in track 114. Differently from Fig. 8, the amplitudes of ATWs during October-December are larger than that during July-

September. It should be attributed to that the monsoon winds in winter are stronger than that in summer.

Lin et al. (2021) investigated the tilt of mean dynamic topography along the coast of the Chinese mainland. Wu (2021) used a nondimensional parameter (Pe_β) to describe the influence of open ocean forcing on shelf circulation, which is determined by the ratio of long-wave-limit planetary to TRW speeds. In this study, $Pe_\beta < 1$, which indicates shelf currents decayed rapidly toward the coast. Their results confirm that the ATWs predict the coastal dynamic topography over the continental shelf of the SCS well.

6 Summary

Using sea level data derived from the tide-gauge stations Kanmen, Xiamen, Shanwei, Hongkong, and Zhapo, this study analyzes statistical features of the CSWs, inter-seasonal and seasonal signals. Meanwhile, along-track SLA data derived from multiple satellite altimeters from 1993 to 2020 are applied to detect the cross-shelf structures of the signals. The major results are summarized as follows.

1) CSWs of periods shorter than 40 d propagate along the coast with the phase speed of about 10 m s^{-1} in the ECS and 8 m s^{-1} in the SCS. The dispersion relation indicates that the waves belong mode 1 CSWs.

2) Owing to the fact that the repeated observation period of the satellite altimeters is comparable with that of CSWs, we combine fragments of the numerous repeated observations of along-track SLA to reconstruct the cross-shelf structure of CSWs. The results show that the maximum amplitudes of CSWs have remarkable seasonal variability, about 0.6 m during July-September, while only 0.2 m during April-June. The reconstructed cross-shelf structures of CSWs confirm the property of mode 1 CSWs. Moreover, the energy is trapped within the partial continental shelf shallower than 200 m.

3) The inter-seasonal and seasonal signals present as ATWs on the continental shelf. The amplitudes of ATWs have remarkable seasonal variability, ~0.10 m during October-December, twice larger than 0.04 m, 0.05 m and -0.06 m during January-March, July-September, and April-June, respectively. These results reveal that the

24

local wind stress substantially influences ATWs on the continental shelf.

4) The results derived from the observation data of along-coast tide-gauge stations combined with cross-shelf tracks of satellite altimeters are interpreted well by the framework of linear wave theory. It implies that the technological approaches developed in this study are suitable for constructing the cross-shelf structures of CSWs and ATWs on the continental shelf.

However, owing to the neglective wind stress and baroclinicity, higher modes of waves are not discussed in this paper. Observations from moorings and numerical models will be used in our future studies to obtain the characteristics of baroclinic coastal trapped waves.

Data Availability Statement

The tide gauge data are available at https://psmsl.org/data/obtaining/. The along-track SLAs is obtained at ftp-access.aviso.altimetry.fr.

Author contributions

JYL were responsible for writing the original draft. Review and editing were conducted by QAZ. Conceptualization was handled by JYL, QAZ and LLX. TH and YX were responsible for data curation. LLX acquired funding.

Competing interests

The contact author has declared that none of the authors has any competing interests.

References:

Aydın, M., Beşiktepe, Ş.T., 2022. Mechanism of generation and propagation characteristics of coastal trapped waves in the Black Sea. Ocean Sci. 18, 1081-1091.

Birol, F., Léger, F., Passaro, M., Cazenave, A., Niño, F., Calafat, F.M., Shaw, A., Legeais, J.-F., Gouzenes, Y., Schwatke, C., Benveniste, J., 2021. The X-TRACK/ALES multi-mission processing system: New advances in altimetry towards the coast. Adv. Space Res. 67, 2398-2415.

Castro, B.M., Lee, T.N., 1995. Wind-forced sea level variability on the southeast Brazilian shelf. Journal of Geophysical Research: Oceans 100, 16045-16056.

Cazenave, A., Moreira, L., 2022. Contemporary sea-level changes from global to local scales: a review. Proceedings of the Royal Society A: Mathematical, Physical and Engineering Sciences 478, 20220049.

Chapman, D.C., 1987. Application of wind-forced, long, coastal-trapped wave theory along the California coast. Journal of Geophysical Research: Oceans 92, 1798-1816.

Chen, D., Su, J., 1987. Continental shelf waves along the coasts of China. Acta Ocean. Sin. 3, 317-334.

Chen, J., Zhu, X.-H., Zheng, H., Nakamura, H., Zhao, R., Wang, M., Park, J.-H., Nishina, A., 2022. Observation of Topographic Rossby Waves Triggered by Kuroshio Path Meander in the East China Sea. Journal of Geophysical Research: Oceans 127, e2022JC018667.

Chen, N., Han, G., Yang, J., Chen, D., 2014. Hurricane Sandy storm surges observed by HY-2A satellite altimetry and tide gauges. Journal of Geophysical Research: Oceans 119, 4542-4548.

Cheng, X., Qi, Y., 2007. Trends of sea level variations in the South China Sea from merged altimetry data. Global and Planetary Change 57, 371-382.

Clarke, A.J., 1977. Observational and Numerical Evidence for Wind-Forced Coastal Trapped Long Waves. J. Phys. Oceanogr. 7, 231-247.

Clarke, A.J., Brink, K., 1985. The response of stratified, frictional flow of shelf and slope waters to fluctuating large-scale, low-frequency wind forcing. J. Phys. Oceanogr. 15, 439-453.

Csanady, G.T., 1978. The Arrested Topographic Wave. J. Phys. Oceanogr. 8, 47-62.

Ding, Y., Bao, X., Shi, M., 2012. Characteristics of coastal trapped waves along the northern coast of the South China Sea during year 1990. Ocean Dyn. 62, 1259-1285.

Ding, Y., Bao, X., Yao, Z., Song, D., Song, J., Gao, J., Li, J., 2018. Effect of coastal-trapped waves on the synoptic variations of the Yellow Sea Warm Current during winter. Cont. Shelf Res. 167, 14-31.

Ding, Y., Yao, Z., Zhou, L., Bao, M., Zang, Z., 2020. Numerical modeling of the seasonal circulation in the coastal ocean of the Northern South China Sea. Frontiers of Earth Science 14, 90-109.

Dukhovskoy, D., Morey, S., 2011. Simulation of the Hurricane Dennis storm surge and considerations for vertical resolution. Nat. Hazards 58, 511-540.

Fang, G., Chen, H., Wei, Z., Wang, Y., Wang, X., Li, C., 2006. Trends and interannual variability of the South China Sea surface winds, surface height, and surface temperature in the recent decade. Journal of Geophysical Research: Oceans 111.

Gan, J., Li, H., Curchitser, E.N., Haidvogel, D.B., 2006. Modeling South China Sea circulation: Response to seasonal forcing regimes. Journal of Geophysical Research: Oceans 111.

Han, G., Ma, Z., Chen, D., deYoung, B., Chen, N., 2012. Observing storm surges from space: Hurricane Igor off Newfoundland. Sci. Rep. 2.

Heaps, N.S., Huthnance, J.M., Jones, J.E., Wolf, J., 1988. Modelling of storm-driven shelf waves north of Scotland—I. Idealized models. Cont. Shelf Res. 8, 1187-1210.

Ho, C.-R., Zheng, Q., Soong, Y.S., Kuo, N.-J., Hu, J.-H., 2000. Seasonal variability of sea surface height in the South China Sea observed with TOPEX/Poseidon altimeter data. Journal of Geophysical Research: Oceans 105, 13981-13990.

Hormazabal, S., Shaffer, G., Letelier, J., Ulloa, O., 2001. Local and remote forcing of sea surface temperature in the coastal upwelling system off Chile. Journal of Geophysical Research: Oceans 106, 16657-16671.

Hsueh, Y., Pang, I.-C., 1989. Coastally Trapped Long Waves in the Yellow Sea. J. Phys. Oceanogr. 19, 612-625.

Hsueh, Y., Romea, R.D., 1983. Wintertime winds and coastal sea-level fluctuations in the Northeast China Sea. Part I: observations. J. Phys. Oceanogr. 13, 2091-2106.

Huang, D., Zeng, D., Ni, X., Zhang, T., Xuan, J., Zhou, F., Li, J., He, S., 2015. Alongshore and cross-shore circulations and their response to winter monsoon in the western East China Sea. Deep Sea Res. Part II.

Kajikawa, Y., Yasunari, T., 2005. Interannual variability of the 10–25- and 30–60-day variation over the South China Sea during boreal summer. Geophysical Research Letters 32.

Li, J., Li, M., Wang, C., Zheng, Q., Xu, Y., Zhang, T., Xie, L., 2023a. Multiple mechanisms for chlorophyll a concentration variations in coastal upwelling regions: a case study east of Hainan Island in the South China Sea. Ocean Sci. 19, 469-484.

Li, J., Zheng, Q., Hu, J., Fan, Z., Zhu, J., Chen, T., Zhu, B., Xu, Y., 2015. Wavelet analysis of coastal-trapped waves along the China coast generated by winter storms in 2008. Acta Ocean. Sin. 34 22-31.

Li, J., Zheng, Q., Hu, J., Xie, L., Zhu, J., Fan, Z., 2016. A case study of winter storm-induced continental shelf waves in the northern South China Sea in winter 2009. Cont. Shelf Res. 125, 127-135.

Li, J., Zheng, Q., Li, M., Li, Q., Xie, L., 2021. Spatiotemporal Distributions of Ocean Color Elements in Response to Tropical Cyclone: A Case Study of Typhoon Mangkhut (2018) Past over the Northern South China Sea. Remote Sensing 13, 687.

Li, J., Zhou, C., Li, M., Zheng, Q., Li, M., Xie, L., 2023b. A case study of continental shelf waves in the northwestern South China Sea. Acta Ocean. Sin.

Li, L., 1993. A study of winter subtidal sea level fluctuation along the northern coast of the South China Sea. Tropic Oceanology.

Lin, W., Lin, H., Hu, J., 2021. The Tilt of Mean Dynamic Topography and its Seasonality Along the Coast of the Chinese Mainland. Journal of Geophysical Research: Oceans 126, e2020JC016778.

Lin, W., Lin, H., Hu, J., Huang, L., 2022. Relative Contributions of Open-Ocean Forcing and Local Wind to Sea Level Variability Along the West Coasts of Ocean Basins. Journal of Geophysical Research: Oceans 127, e2022JC019218.

Lin, X., Yang, J., 2011. An asymmetric upwind flow, Yellow Sea Warm Current: 2. Arrested topographic waves in response to the northwesterly wind. Journal of Geophysical Research: Oceans 116.

Lin, X., Yang, J., Guo, J., Zhang, Z., Yin, Y., Song, X., Zhang, X., 2011. An asymmetric upwind flow, Yellow Sea Warm Current: 1. New observations in the western Yellow Sea. Journal of Geophysical

Research: Oceans 116.

Marshall, A.G., Hendon, H.H., 2013. Impacts of the MJO in the Indian Ocean and on the Western Australian coast. Clim. Dyn., 1-17.

Morey, S.L., Baig, S., Bourassa, M.A., Dukhovskoy, D.S., O'Brien, J.J., 2006. Remote forcing contribution to storm-induced sea level rise during Hurricane Dennis. Geophys. Res. Lett. 33.

Mysak, L.A., 1980. Topographically trapped waves. Annual Review of Fluid Mechanics 12, 45-76.

Quan, Q., Cai, Z., Jin, G., Liu, Z., 2021. Topographic Rossby Waves in the Abyssal South China Sea. J. Phys. Oceanogr. 51, 1795-1812.

Robinson, A., 1964. Continental shelf waves and the response of sea level to weather systems. J. Geophys. Res. 69, 367-368.

Rong, Z., Liu, Y., Zong, H., Cheng, Y., 2007. Interannual sea level variability in the South China Sea and its response to ENSO. Global and Planetary Change 55, 257-272.

Schulz, W.J., Mied, R.P., Snow, C.M., 2011. Continental shelf wave propagation in the Mid-Atlantic Bight: a general dispersion relation. J. Phys. Oceanogr. 42, 558-568.

Shen, J., Zhang, S., Zhang, J., Zeng, M., Fang, W., 2021. Observation of continental shelf wave propagating along the eastern Taiwan Strait during Typhoon Meranti 2016. Journal of Oceanology and Limnology 39, 45-55.

Thiebaut, S., Vennell, R., 2010. Observation of a fast continental shelf wave generated by a storm impacting Newfoundland using wavelet and cross-wavelet analyses. J. Phys. Oceanogr. 40, 417-428.

Vialard, J., Shenoi, S., McCreary, J., Shankar, D., Durand, F., Fernando, V., Shetye, S., 2009. Intraseasonal response of the northern Indian Ocean coastal waveguide to the Madden-Julian Oscillation. Geophys. Res. Lett. 36.

Vignudelli, S., Birol, F., Benveniste, J., Fu, L.-L., Picot, N., Raynal, M., Roinard, H., 2019. Satellite Altimetry Measurements of Sea Level in the Coastal Zone. Surv. Geophys. 40, 1319-1349.

Wang, B., Huang, F., Wu, Z., Yang, J., Fu, X., Kikuchi, K., 2009. Multi-scale climate variability of the South China Sea monsoon: A review. Dyn. Atmos. Oceans 47, 15-37.

Wang, D.-P., Mooers, C.N., 1976. Coastal-trapped waves in a continuously stratified ocean. J. Phys. Oceanogr. 6, 853-863.

Wang, H., Li, W., Xiang, W., 2022. Sea level rise along China coast in the last 60 years. Acta Oceanologica Sinica 41, 18-26.

Wang, H., Liu, K., Gao, Z., Fan, W., Liu, S., Li, J., 2017. Characteristics and possible causes of the seasonal sea level anomaly along the South China Sea coast. Acta Oceanologica Sinica 36, 9-16.

Wu, H., 2021. Beta-Plane Arrested Topographic Wave as a Linkage of Open Ocean Forcing and Mean Shelf Circulation. J. Phys. Oceanogr. 51, 879-893.

Xie, L., Zheng, Q., Zhang, S., Hu, J., Li, M., Li, J., Xu, Y., 2018. The Rossby normal modes in the South China Sea deep basin evidenced by satellite altimetry. International Journal of Remote Sensing 39, 399-417.

Xu, Y., Lin, M., Zheng, Q.a., Song, Q., Ye, X., 2016. A study of sea level variability and its long-term trend in the South China Sea. Acta Oceanologica Sinica 35, 22-33.

Yin, L., Qiao, F., Zheng, Q., 2014. Coastal-trapped waves in the East China Sea observed by a mooring array in winter 2006. J. Phys. Oceanogr. 44, 576-590.

Zhao, R., Zhu, X.-H., Park, J.-H., 2017. Near 5-Day Nonisostatic Response to Atmospheric Surface Pressure and Coastal-Trapped Waves Observed in the Northern South China Sea. J. Phys. Oceanogr. 47, 2291-2303.

724 Zheng, Q., Hu, J., Zhu, B., Feng, Y., Jo, Y.-H., Sun, Z., Zhu, J., Lin, H., Li, J., Xu, Y., 2014. Standing
725 wave modes observed in the South China Sea deep basin. Journal of Geophysical Research: Oceans 119,
726 4185-4199.

727 Zheng, Q., Zhu, B., Li, J., Sun, Z., Xu, Y., Hu, J., 2015. Growth and dissipation of typhoon-forced solitary
728 continental shelf waves in the northern South China Sea. Clim. Dyn. 45, 853-865.

729 Zhou, C., Li, J., Zheng, Q., Xie, L., 2023. Characteristics of winter continental shelf waves in the northern
730 South China Sea. Journal of Guangdong Ocean University 43, 89-97.

731 Zhuang, W., Xie, S.P., Wang, D.X., Taguchi, B., Aiki, H., Sasaki, H., 2010. Intraseasonal variability in
732 sea surface height over the South China Sea. Journal of Geophysical Research-Oceans 115.

733

734